Study of particle migration and deposition in mixed convective pipe flow of nanofluids at different inclination angles

Mostafa Mahdavi[1], I. Garbadeen[1], Mohsen Sharifpur[1], Mohammad Hossein Ahmadi[2] and Josua P. Meyer[1]

[1]Department of Mechanical and Aeronautical Engineering, University of Pretoria, Pretoria, 0028, South Africa
[2]Faculty of Mechanical Engineering, Shahrood University of Technology, Shahrood, Iran

*Correspondence to Mohsen Sharifpur (mohsen.sharifpur@up.ac.za) or Mohammad Hossein Ahmadi (mohammadhosein.ahmadi@gmail.com)

Abstract

Mixed convection flow of aluminium-oxide nanoparticles in water through a circular tube was modelled using the discrete phase model and implemented on ANSYS-Fluent 17.0 through customised user-defined functions. The inclination angle was varied to study its effect on the migration and deposition of the nanoparticles. Experimentally determined thermo-physical properties were used in the analysis instead of theoretical or empirical models from the literature. Varying inclination angles were found to significantly affect the migration and deposition of nanoparticles. A critical angle of maximum deposition of approximately 30° was found for volume concentrations 1%, 3% and 5%. The effect of varying inclination angle on the heat transfer coefficient was minimal for low angles of inclination between 0 and 35% and decreased significantly after 40%. The effect of Saffman's lift, thermophoretic, Magnus and Brownian effects were also investigated, and results show that thermophoretic and Brownian effects were most dominant effects.

Keywords: Nanoparticles; Mixed convection; Inclination angle; Discrete modelling; ANSYS-Fluent; UDFs

List of symbols

C_c	Cunningham correction factor
C_D	Drag coefficient
C_{ML}	Rotational coefficient
C_ω	Rotational drag coefficient
c_p	Specific heat (J/kg K)
d_p	Particle diameter (m)
d_0	Equilibrium distance (m)
D_T	Thermophoresis coefficient
F_B	Brownian force (m s^{-2})
F_T	Thermophoresis force (m s^{-2})
F_M	Magnus force (m s^{-2})
F_L	Lift force (m s^{-2})
F_D	Drag force (m s^{-2})
F_{bind}	Adhesion force (m s^{-2})
F_{VDW}	Van der Waals force (m s^{-2})
h	Heat transfer coefficient (W/m^2 K)
H	Hamaker constant (J)
Gr	Grashof number
G_w	Gaussian weight function
I_p	Moment of inertia (kg m^{-2})
d	Tube inner diameter (m)
k	Thermal conductivity (W/m K)
Kn	Knudsen number
K_B	Boltzmann constant (m^2 kg/°K s^2)
m_p	Particle mass (kg)
$N_{particle}$	Number of particles
r	Radial coordinate (m)
Re_p	Particle Reynolds number
Re_{ω_p}	Rotational Reynolds number
Ri	Richardson number
T	Temperature (K)
Δt_p	Particle time step (s)
V, u	Velocity (m s^{-1})

Greek letters

α	Inclination angle (°)
μ_c	Fluid viscosity (Pa s)
λ	Mean free path (m)
ω_p	Particle angular velocity (1 s^{-1})
$\mathbf{\Omega}$	Relative particle–liquid angular velocity (1 s^{-1})
ρ	Density (kg m^{-3})
τ	Particle relaxation time (s)

θ_{particle} Particle variable
$\overrightarrow{\zeta_i}$ Random function

Subscripts

f, c Fluid
p Particle

Introduction

Researchers have extensively studied nanofluids over the past 3 decades both analytically and experimentally to formulate a more rigorous understanding of their properties—the most widely studied being thermal conductivity. Several studies [1–7] have reported enhancement in heat transfer performance and speculated over their viability as a replacement for conventional heat transfer fluids. However, to consider nanofluids for use in practical applications, it is necessary to also understand the migration and deposition of nanoparticles in mixed convective flow and their effects on the heat transfer performance and pressure variation. Numerous studies into nanofluids have thus far focused on thermal conductivity with fewer studies into the mixed behaviour of nanofluids [8, 9]. Of the studies conducted into nanofluids in mixed convective flow, the single-phase model has been favoured over the discrete phase and mixture model for its simplicity and quick results.

The thermo-physical properties used in modelling are often determined using empirical or theoretical models from the literature which are known to have significant discrepancies in results [10–15]. The single-phase model assumes a homogeneous particle distribution with zero slip velocity between fluid and particle and fails to account for the particle–fluid or particle–particle interactions which are necessary for studying the migration and deposition of particles. Similarly, the Eulerian–Eulerian and mixture model which models nanofluids as a single fluid with two phases able to move at different velocities assumes negligible fluid–particle interactions and would also be inadequate primarily due to the requirement of defining solid viscosities for the nanoparticles. This introduces uncertainty in the overall dynamic viscosity of the nanofluid. Behzadmehr et al. [16], for example, used this approach and applied Miller and Gidaspow's solid viscosity model for the nanoparticles which Genasan et al. [17] stated was originally developed for modelling solidus viscosity in dense gas–solid flow inside a vertical tube. Results by Ding and Wen [18] report the non-uniform distribution of nanoparticles across the flow cross section with higher particle concentrations found around the centreline of the pipe than the near the wall region [19]. Pakravan and Yaghoubi [20] and Garoosi et al. [21] have all reported the non-uniform distribution of nanoparticles using the mixture model. Studies by Aminfar and Motallebzadeh [19] also show the non-uniform distribution of nanoparticles as affected by Brownian motion and thermophoretic effects using Lagrangian–Eulerian approach and found that the Brownian forces were the most dominant in affecting nanoparticle distribution. This finding confirms Buongiorno [22] findings that the main forces affecting nanoparticle distribution were Brownian and thermophoretic and that these were more significant in laminar flow regimes compared to turbulent.

An appropriate model to study particle migration and deposition would, therefore, be the two-phase discrete phase model (DPM) which has begun to be used in recent years. This model allows for the Lagrangian tracking of the nanoparticles in a Eulerian described fluid field with thermo-physical property inputs separately specified for each phase. This is a significant advantage over other models because true properties are retained as opposed to using approximate thermo-physical models. Other factors affecting particle motion like drag force, gravity, Brownian motion, sedimentation, layering at solid–fluid interface, thermophoresis can be systematically included in the analysis and their effects evaluated Differences in results based on choice of model can lead to 11% deviation in the average heat transfer coefficient as reported by Bianco et al. [23] and Moraveji and Esmaeili [24] when comparing single-phase and DPM approaches using alumina–water nanofluid in laminar forced convection flow. Numerical studies by Mojarrad et al. [25] of alumina–water nanofluids in laminar convective flow compared the single, mixture and discrete phase models and found that DPM showed most agreement with experimental data. Bahremandi et al. using silver–water nanofluids compared the single- and discrete phase models and reported the later as more accurate when compared to experimental results. Nevertheless, it is worth noting that Kumar and Puranik [23] found the single-phase model to be more accurate than the discrete phase model for particle volume concentration greater than 0.5%. This could be due to the choice of thermo-physical model used and the set of experimental results to which the different models were compared to usually without a complete justification.

However, most studies using DPM have been limited to heat transfer and convection flow, while few studies have been dedicated to particle distribution in mixed convection flow. Mixed convection has a wide application in industries where a significant heat transfer across boundaries occurs simultaneously with fluid flow. Furthermore, the pipe networks and fluid flow in industrial applications are not always parallel nor orthogonal to gravity. This study, therefore, considers the particle migration and deposition in mixed flow in circular tubes oriented at different angles

using the Lagrangian–Eulerian DPM model in fully developed laminar flow and implemented using the commercial CFD software ANSYS 17.0. Several slip mechanisms which cause relative velocities between particle and fluid are compared to evaluate their significance and their effect on particle migration and particle distribution.

Mathematical modelling

Nanofluid thermo-physical properties

The working fluid is a colloidal solution of Al_2O_3 particles of average diameter 30 nm in water. Volume concentrations of 1, 3 and 5% were considered, and thermo-physical properties of the nanofluids are shown in Table 1.

Geometry

Figure 1 shows the geometric set-up under investigation. It consists of an axis-symmetric flow in a circular tube of 6.35 mm inside diameter, d, and inclined downwards at varying angle α. An adiabatic region of length 318 mm precedes a 1270-mm-long constant-wall-temperature section of the tube. This allows the flow to fully develop before entering the heated section of the tube.

Using the assumption of a fully developed flow at the start of the heated section, the velocity profile V is given by

$$V = 2\bar{V}\left(1 - \frac{4r^2}{d^2}\right) \tag{1}$$

where the average velocity and radius are $\bar{V}$ and r, respectively.

Governing equations

Analysis of the two-phase flow and heat transfer is carried out by applying the Eulerian frame of reference to the continuous phase and solving the familiar continuity, momentum and energy equations. The nanoparticle motions are solved separately in the Lagrangian frame using Newton's third law of motion. The solutions are coupled with the momentum and energy equations by introducing the source terms S_m and S_e which represent the transfer of momentum and heat, respectively, between the continuous and the discrete phases.

$$\nabla \cdot \left(\rho \vec{V}\right) = 0 \tag{2}$$

$$\nabla \cdot \left(\rho \vec{V}\vec{V}\right) = -\nabla P + \nabla \cdot \left(\mu \nabla \vec{V}\right) + S_m \tag{3}$$

$$\nabla \cdot \left(\rho \vec{V} C_p T\right) = \nabla \cdot (k \nabla T) + S_e \tag{4}$$

The source term S_m is evaluated as follows [23]:

$$S_m = \sum_n \frac{m_p}{\delta V} \frac{\mathrm{d}\overrightarrow{V_p}}{\mathrm{d}t} \tag{5}$$

where n is the number of particles within a given cell volume δV. $\frac{\mathrm{d}\overrightarrow{V_p}}{\mathrm{d}t}$ is the instantaneous rate of change of velocity which represents of a number of forces:

$$\frac{\mathrm{d}\overrightarrow{V_p}}{\mathrm{d}t} = \overrightarrow{F_D} + \overrightarrow{F_G} + \overrightarrow{F_L} + \overrightarrow{F_T} + \overrightarrow{F_M} + \overrightarrow{F_B} \tag{6}$$

The forces terms listed on the right-hand side are the drag, gravitational, Saffman's lift, thermophoretic, Magnus and Brownian forces, respectively. The effects of virtual mass and pressure gradient forces are considered negligible [26]. To relate particle force balance equation to other fluid equations, it can be explained that calculating forces acting

Table 1 Thermo-physical properties of nanofluid components

Component	Density/kg m^{-3}	Thermal conductivity/W/m K	Specific heat/J/kg K
Water	998.2	0.6	4181
Al_2O_3	3880	36	773

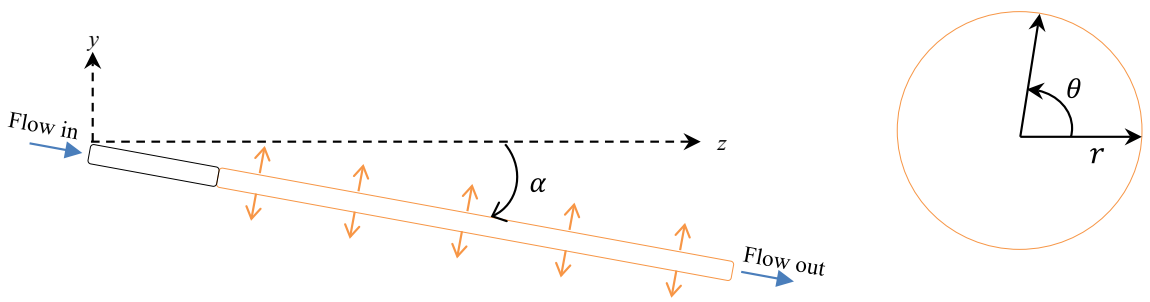

Fig. 1 Geometry of model: *a* side section and *b* cross section

on particles in Eq. (6), the trajectory and velocity field of the particles are obtained. Then, all the information about particles is used to calculate the momentum source term in Eq. (5). Eventually, this term is replaced in momentum Eq. (3).

The fluid exerts a viscous drag force $\overrightarrow{F_D}$ on the particles and is determined by Stoke's law [25]

$$\overrightarrow{F_D} = \frac{18}{d_p^2 \rho_p C_c}\left(\vec{V} - \overrightarrow{V_p}\right) \tag{7}$$

where the Cunningham slip correction factor, C_c (for slip boundary conditions), is given by

$$C_c = 1 + \frac{2\lambda}{d_p}\left(1.257 + 0.4e^{-1.1 d_p/2\lambda}\right) \tag{8}$$

The Knudsen number, Kn, is given by λ/d_p, where λ denotes the mean free path of 0.3 nm in this study. Since $Kn \ll 0.1$, the Cunningham slip correction factor can be approximated as $C_c \approx 1$. This indicates that the difference between drag forces near the wall and away from the wall is negligible due to the small particle sizes involved. The dominant particle–wall interaction would therefore be wall capture and rebounding.

The gravitational force is given by:

$$\overrightarrow{F_G} = \frac{\vec{g}(\rho_p - \rho_f)}{\rho_p} \tag{9}$$

The Saffman's lift force is denoted by F_L and represents the force on a particle in a shear stress field. This force decreases with distance away from the wall [27] and is important when analysing particle–wall collisions [28, 29]:

$$\overrightarrow{F_L} = \frac{2K_s v^{1/2}\sigma_{ij}}{\rho_p d_p (\sigma_{ij}\sigma_{ij})^{1/4}}\left(\vec{V} - \vec{V}_p\right) \tag{10}$$

where the tensor σ_{ij} denotes the deformation and K_s is a constant equal to 2.594.

Particles in flow regions where there exists a temperature gradient around the sides of the particles cause a differential on molecular velocities around the particle which results in a force that pushes particles towards the lower temperature side. This effect is referred to as thermophoresis and is given by [30]:

$$\overrightarrow{F_T} = -D_T \frac{\vec{\nabla} T}{T} \tag{11}$$

$$D_T = 0.78 \frac{\pi \mu_c^2 d_p}{\rho_c} \frac{k_c}{2k_c + k_p} \tag{12}$$

Lift force induced by particle rotation about its axis in a uniform flow field is referred to a Magnus force, and the effect is magnified in highly rotational flow fields. The following set of equations define the Magnus force [31]:

$$\overrightarrow{F_M} = \frac{1}{2} A_p C_{ML} \rho_c \frac{\left|\vec{V} - \vec{u}_p\right|}{\left|\vec{\Omega}\right|}\left[\left(\vec{V} - \overrightarrow{u_p}\right) \times \vec{\Omega}\right] \tag{13}$$

$$\vec{\Omega} = \frac{1}{2}\nabla \times \vec{V} - \overrightarrow{\omega_p} \tag{14}$$

$$C_{ML} = 0.45 + \left(\frac{Re_{\omega_p}}{Re_p} - 0.45\right)\exp\left(-0.05684 Re_{\omega_p}^{0.4} Re_p^{0.3}\right) \tag{15}$$

$$Re_{\omega_p} = \frac{\rho_c |\Omega| d_p^2}{4\mu_c} \tag{16}$$

where projected particle surface area and the rotational lift coefficient are A_p and C_{ML}, respectively. Solving the angular momentum equation yields the angular velocity of the particle:

$$I_p \frac{d\omega_p}{dt_p} = \frac{\rho_p}{2}\left(\frac{d_p}{2}\right)^5 C_\omega \Omega \tag{17}$$

$$I_p = \frac{\pi}{60}\rho_p d_p^5 \tag{18}$$

$$C_\omega = \frac{6.45}{\sqrt{Re_{\omega_p}}} + \frac{32.1}{Re_{\omega_p}} \tag{19}$$

An additional term F_B to account for Brownian motion—the random motion of particles in a fluid dependent of the temperature and kinetic energy of the particles [29] and can be expressed as:

$$\overrightarrow{F_B} = \overrightarrow{\zeta_i}\sqrt{\frac{6\pi d_p \mu_c K_B T}{\Delta t_p}} \tag{20}$$

where ζ_i denotes the unit-variance random number generated from Gaussian white noise operation with mean value zero.

Lastly, assuming negligible radiation transfers and internal particle thermal resistance the energy transfer between the particles and the base fluid implemented on ANSYS-Fluent through UDF takes the form below:

$$m_p c_{p,p} \frac{dT_p}{dt} = m_c c_{p,c} \frac{DT_c}{Dt_p} - 2\pi d_p k_c (T_p - T_c) \tag{21}$$

where mass m_c represents the mass of fluid displaced by a particle and therefore the material derivative term on the right-hand side is the heat transfer between the displaced fluid and the nanoparticle. The second term is the heat transfer by conduction between the surface of the nanoparticle and the surrounding fluid in contact with the particle. Knowing the particles temperature, the heat source term in fluid heat transfer (Eq. 4) is easily calculated.

Numerical analysis

Laminar mixed convection heat transfer of alumina–water nanofluid of volume concentrations 1, 3 and 5% in a cooling circular tube at different angles α was investigated. The uniform circular geometry lends itself well to structure meshing, thereby allowing for quicker solution convergence. Although the flow is limited to the laminar regime which may indicate a low cell number requirement, the mesh must cater for the large number of particles that are to be tracked in the Lagrangian frame. To adequately capture boundary conditions, finer mesh sizes were used near the wall. In this study, a mesh independence analysis was done using particle percentage wall deposition as the convergence criterion. The several meshes tested are presented in Table 2.

The numerical solution was obtained using the commercial solver ANSYS-Fluent 17.0 which allows for user-defined functions (UDF) to be added to the solution process. The energy equation was implemented via UDF. To improve solution convergence of the discrete phase model of nanofluid, the numerical method needed to be carefully selected. In this study, volume discretisation of the governing equation was used. The SIMPLE algorithm for pressure–velocity coupling was used for the convective and diffusive terms. The QUICK scheme was used to implement nanofluid volume fraction, and the second-order upwind was used for interpolation. However, the second-order upwind together with the PRESTO scheme provided divergent pressure solutions for higher nanofluid volume concentration. Therefore, the standard scheme was used instead. Furthermore, the relaxation factors needed to be lowered to allow for quicker convergence.

The momentum and energy equations are solved for a single point-particle in a cell volume which acts as a representative of all particles in the given cell volume. The cell volume is small enough to consider the distribution effect of particles in the cell to be negligible and therefore not included in the solution process. For this approach, the node-based averaging method is most appropriate when mapping the Lagrangian frame onto the Eulerian field and the Gaussian distribution function is used to interpolate the impact of neighbouring cell volumes on the centroid of the given cell [32]

$$\theta_{\text{cell}} = \sum N_{\text{p}} G_{\text{w}} \theta_{\text{p}} \tag{22}$$

$$G_{\text{w}} = \left(\frac{a}{\pi}\right)^{\frac{3}{2}} \exp\ \left(-a \frac{\left|x_{\text{cell}} - x_{\text{p}}\right|^2}{\Delta x^2}\right) \tag{23}$$

where N_{p}, G_{w}, θ_{p} Δx, x_{cell} and x_{p} are the number of particles in the cell, Gaussian weight function, particle variable in the node, characteristic length of the cell, cell location in the neighbourhood and particle location in cell, respectively. There are 26 neighbourhood the cells for the 3D structured the quad mesh.

Analysis of particle–wall interaction can be complex due to the various forces involved. However, due to the nanoscale of particles involved the Van der Waals attraction force plays the dominant role in binding particles to the wall. The gravitational force from Eq. (9) should also be considered since the curvature of the wall results in a component of the gravitational force that is directed towards the wall. This force component can be determined by taking the dot product of the gravitational force vector and the area normal vector.

The total binding force experienced by a particle to the wall can, therefore, be approximated as the sum of gravitational forces and the Van der Waals force. Assuming the circular wall can be approximated as a flat surface in relation to the nanoscale of the particle, the binding force, F_{bind}, can be defined as [33]:

$$F_{\text{bind}} = F_{\text{G}} + F_{\text{VDW}} \tag{24}$$

$$F_{\text{VDW}} = \frac{H d_{\text{p}}}{12 d_o^2} \tag{25}$$

where H and d_{o} denote the Hamaker constant and equilibrium distance between nanofluid and particle [33].

Forces that counter the effect of Eq. (25) or unbind particles to the wall thereby causing them to lift off include the Saffman's lift force, thermophoretic force and Brownian motion as defined in Eqs. (10), (11) and (20), respectively. The Magnus force is omitted as particles in contact with the wall can be assumed to be irrotational. It should also be noted that taking the Brownian motion as an unbinding force is a useful simplification due to its randomness which means the net effect is directed away from the way.

$$F_{\text{unbind}} = F_{\text{L}} + F_{\text{T}} + F_{\text{B}} \tag{26}$$

The net effect of the binding and unbinding forces in relation to the wall determines whether a given particle attaches or detaches from the wall after each particle–wall interaction.

Table 2 Mesh independence study

Number of cells	Deposition/%	Deviation from selected grid/%
33,000	19.5% ± 0.3%	18.0
189,000	18.2% ± 0.2%	10.1
420,000	17.4% ± 0.2%	4.2
678,300	16.7% ± 0.2%	–
1,170,000	16.5% ± 0.2%	1

Considering the order of magnitudes involved in the forces described in Eqs. (24) and (26), it can be expected that $F_{\text{bind}} > F_{\text{unbind}}$. This is because the order of magnitudes of the Hamaker constant and the equilibrium distance are 10^{-20} and 1 A$^{\circ}$, respectively, which results in an overall order of magnitude for the F_{VDW} of 10^{-9}. The gravitational force has order of magnitude 10^{-22} and is negligible when compared to the F_{VDW}. The schematic of important deposition forces is illustrated in Fig. 2.

Boundary conditions

From Fig. 1, the adiabatic entrance region of the tube for flow to fully develop is 318 mm. Inlet temperature at heat transfer region of the tube for both base fluid and particle is uniformly distributed across the cross section. No-slip condition at the wall is applied to both the particles and base fluid. The flow is assumed fully developed at the outlet. The following boundary equations apply:

Inlet: $u = U_{\text{o}} = 0.043$ m/s, $T = T_{\text{o}} = 85\,^{\circ}\text{C}$
Adiabatic wall: $\partial T/\partial r = 0$ for $0 \leq z \leq 318$ mm
Uniform wall temperature: $T = T_{\text{w}} = 24.5\,^{\circ}\text{C}$ for $318 \leq z \leq 1270$ mm

Validation

Validation of the code used in the numerical analysis was done by comparing the heat transfer coefficients for flow through the circular tube at $\alpha = 0^{\circ}$ with experimental results as reported by Mansour et al. [34] using the same nanofluid and volume concentrations. The boundary conditions are similar to the experiments by Mansour et al. [34]. From Table 3, a good agreement was achieved with experimental results with maximum deviation of only 5.7%. Numerical analysis under-reported experimental values; however, experimental values had a maximum uncertainty of 6.28%.

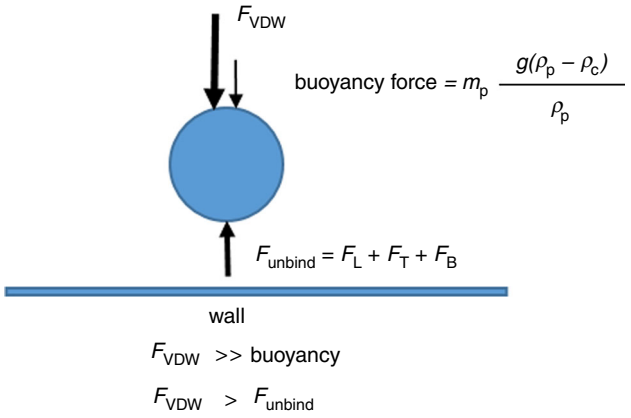

Fig. 2 Schematic of binding and unbinding forces acting on particles

Table 3 Simulated and experimental results of mean heat transfer coefficient of nanofluid flow through circular tube at angle $\theta = 0$, mass flow rate 0.0018 kg s^{-1}, Reynolds number 400 and volume concentrations 0, 2 and 4%

Volume concentration/%	Experimental h/W/m K	Numerical h/W/m K	Error/%
0	859	814	5.2
2	805	768	5.6
4	770	726	5.7

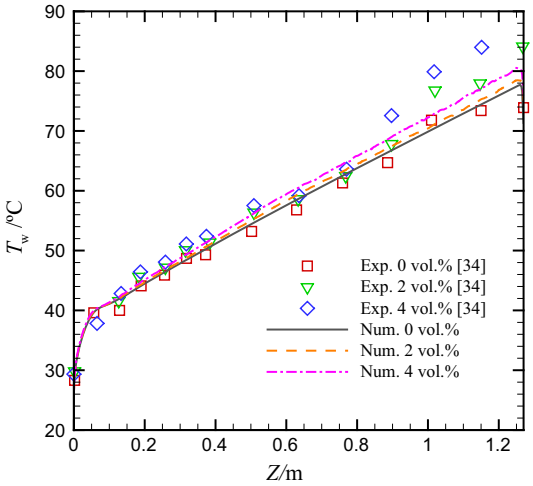

Fig. 3 Experimental and numerical results of variation of wall temperature T_{w} along the pipe length Z for particle volume concentrations 0%, 2% and 4%

The wall temperature along the pipe length is also used for validation, and Fig. 3 shows a comparison between experimental [34] and numerical results of the variation of wall temperature along the pipe length for various particle volume concentrations. Figure 3 shows there is a very good agreement within 6% between experimental and numerical results. Lower particle volume concentrations and smaller axial distances show even better agreement between experimental and numerical results.

Results and discussion

The numerical analysis as described in Sect. 2.4 above was completed using ANSYS-Fluent 17.0 for various inclination angles. Figure 4a shows the distribution of nanoparticles at cross section taken at lengths 0.1, 0.6 and 1.2 m of the tube length for Richardson number, $Ri = \frac{Gr}{Re^2} = 0.019$, 1% volume concentration at 0° inclination angle. It can be observed that areas of high particle concentration develop

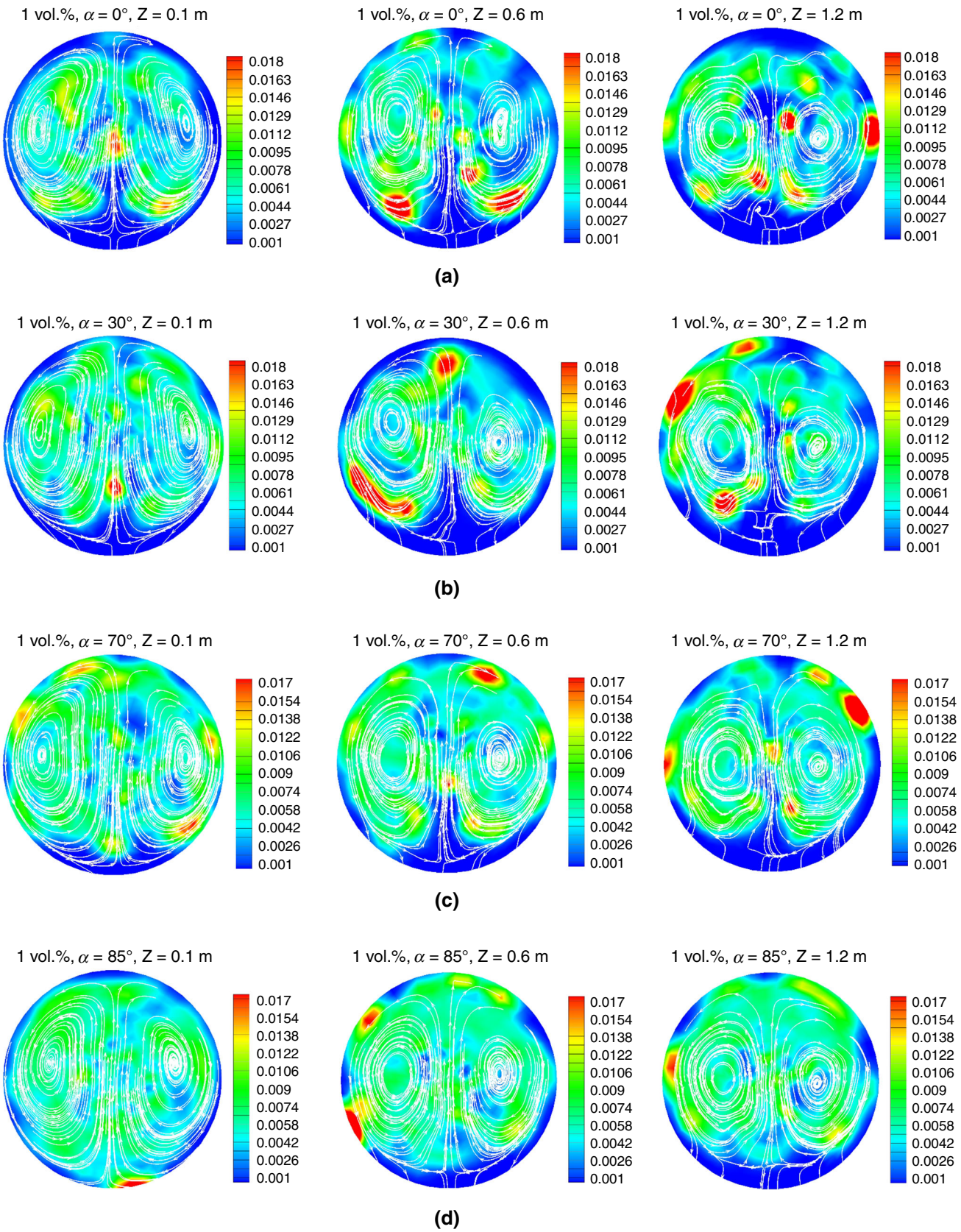

Fig. 4 Flow of nanofluid volume concentration 1% axial distance Z of 0.1, 0.6, 1.2 m. **a** $\alpha = 0°$, **b** $\alpha = 30°$, **c** $\alpha = 70°$ and **d** $\alpha = 85°$

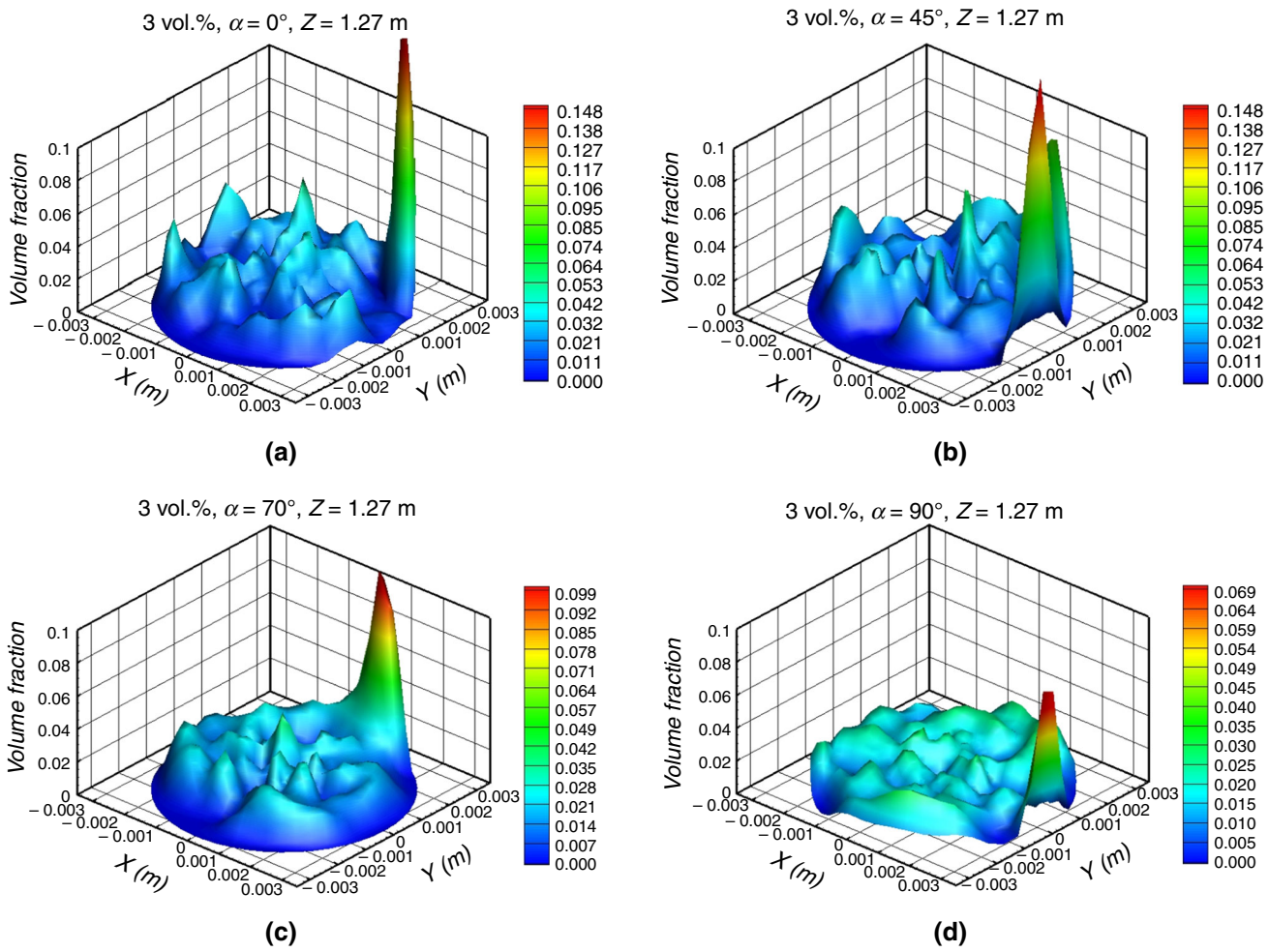

Fig. 5 Nanoparticle distribution for 3% volume concentration at the outlet axial distance $Z = 1.27$ m for inclinations angles. **a** $\alpha = 0°$, **b** $\alpha = 10°$, **c** $\alpha = 70°$ and **d** $\alpha = 90°$

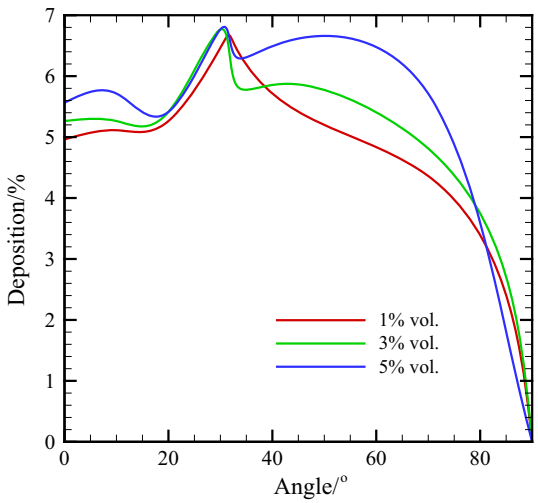

Fig. 6 Variation of percentage particle deposition with increasing inclination angle at volume concentrations 1%, 3% and 5%

as the fluid progresses along the pipe and that they occur nearer to the wall than the central region. This may increase the likelihood of wall erosion and pipe clogging. There is a marked reduction of the nanoparticle presence around the top and bottom wall regions which becomes more significant as the flow progresses through the pipe length. The same observation is made for higher inclination angles as shown in Fig. 4b–d. All nanoparticle concentra-tion hot spots occur near the wall which may indicate the effect of secondary flows which moves nanoparticles towards the wall and the significance of the Van der Waals forces which attaches particles to the wall.

Comparing nanoparticle concentration at each different axial distance in Fig. 4a–d shows that increasing inclina-tion angle increases the area distribution of nanoparticles. This is most prominent for axial distance $Z = 0.1$ where nanoparticles occupation area increased from 80 to 97% of the cross-sectional area when inclination increased from 0°

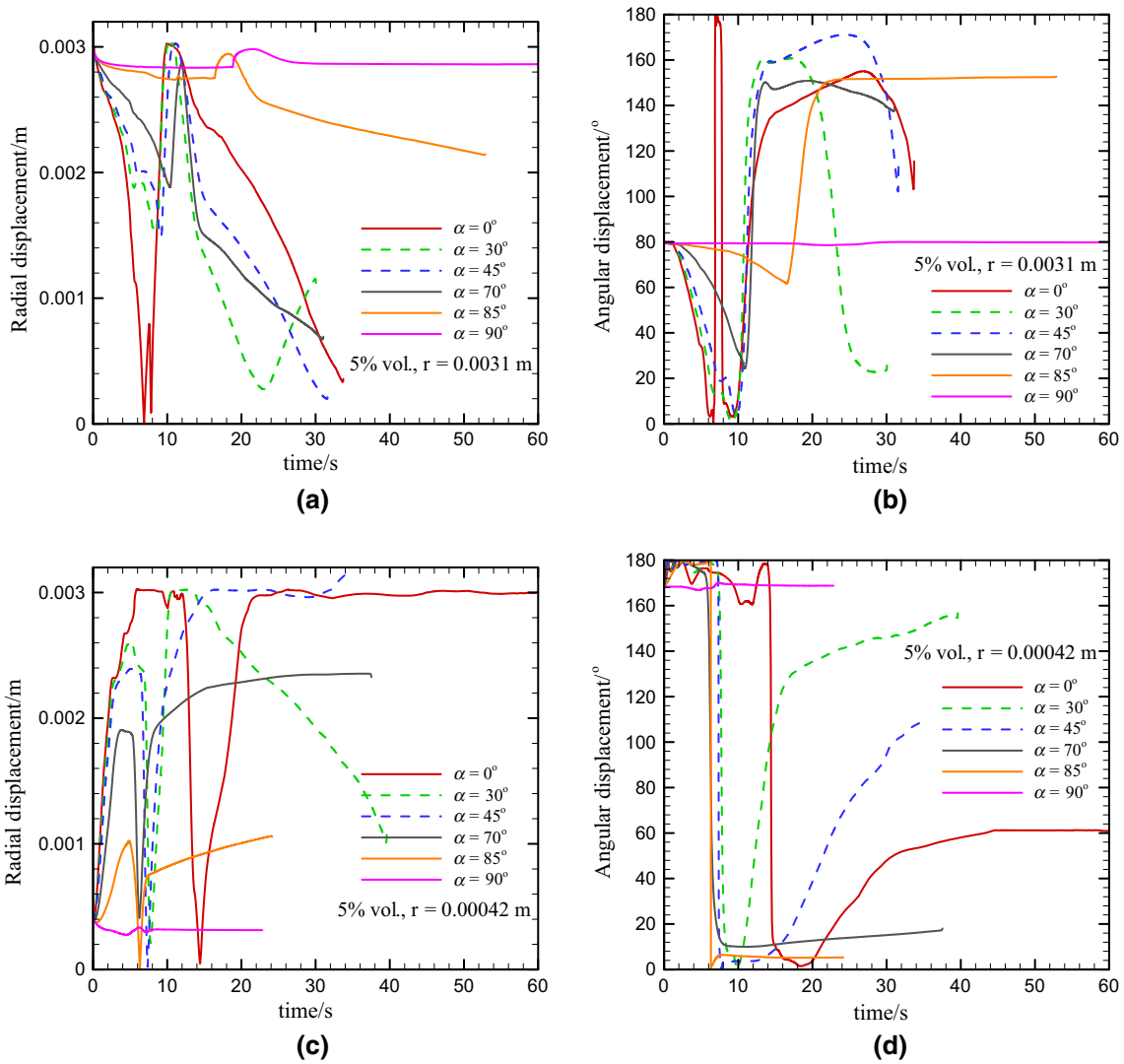

Fig. 7 Change in nanoparticle position in fluid field with time for 5%volume concentration and inclination angle α from 0° to 90°. **a** Change in radial position with time for particle release at radial distance $r = 0.0031$ m. **b** Change in angular position with time for particle release at radial distance $r = 0.0031$ m. **c** Change in radial position with time for particle release at radial distance $r = 0.0041$ m. **d** Change in radial position with time for particle release at angular distance $r = 0.0041$ m

to 85°. This shows that intermediate inclination angles between horizontal and vertical positions are not suitable for achieving maximum particle distribution. This can be attributed to the strong effect of buoyancy force in the horizontal situation compared to other angles towards the vertical situation.

Figure 5 shows the nanoparticle distribution at the exit cross section for various inclination angles from 0° to 90°. It can be observed that the highest particle concentration area is located near the wall region and in the upper half of the cross section. However, the magnitude of maximum particle concentration reduces significantly with increasing inclination angle. This reduction can be related to the changes in mixed convection nature from horizontal to vertical.

The variation of percentage particle deposition with increasing inclination angle at various particle volume concentrations is shown in Fig. 6. The overall trend shows particle deposition decreases with increasing inclination angle. This change can be attributed to the reduction in secondary flow effects which are important in transporting particles to areas near the wall region before the adhesive Van der Waals forces can take effect. It is also important to note the existence of a critical angle of $\alpha \approx 30°$ where particle deposition is maximised. In this study, the angle of maximum particle deposition is observed to be invariant with particle volume concentration. Determining the angle

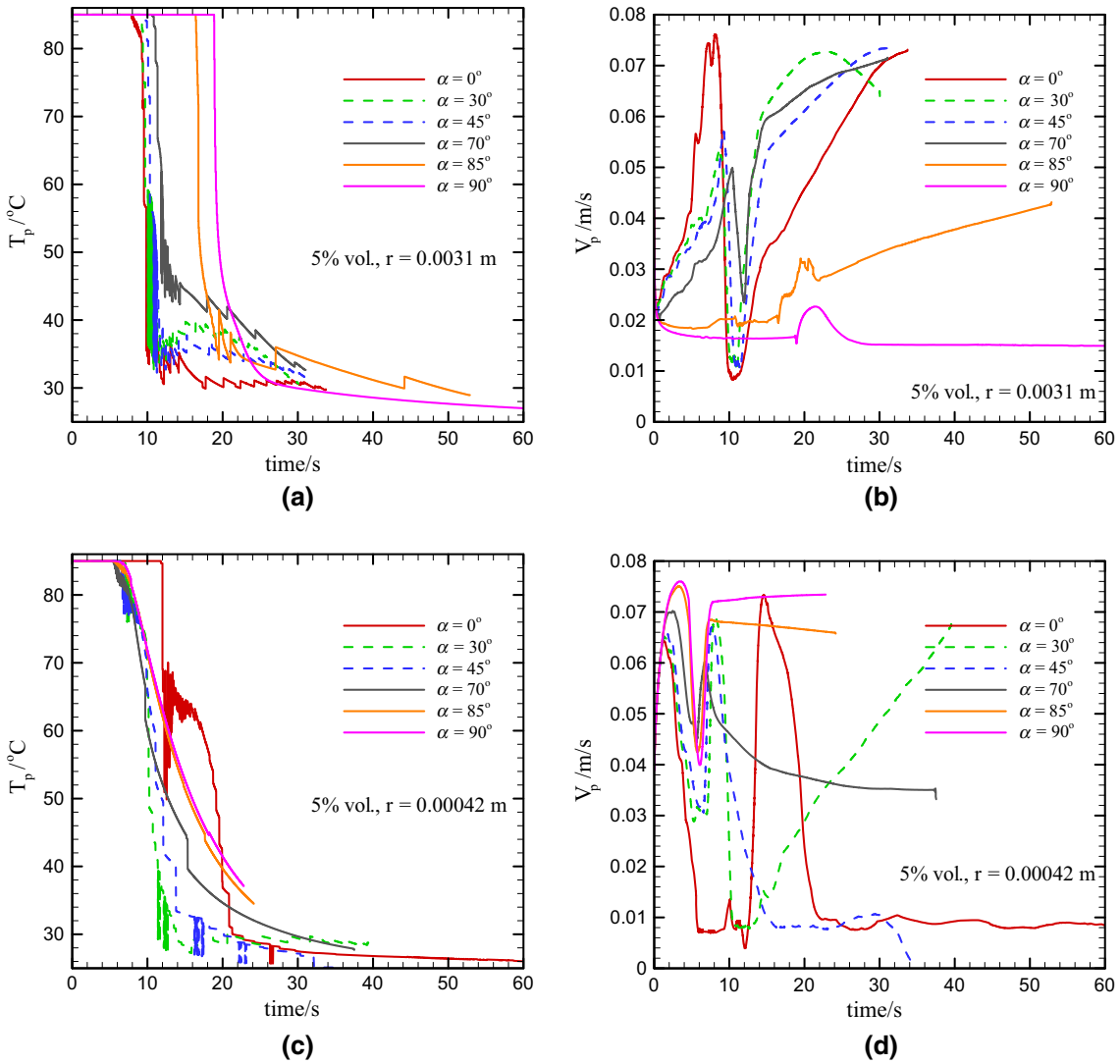

Fig. 8 Particle temperature and velocity for 5% particle volume concentration, $0 \leq \alpha \leq 90°$. **a** Change in temperature with time for particle release at radial distance $r = 0.0031$ m. **b** Change in velocity with time for particle release at radial distance $r = 0.0031$ m. **c** Change in temperature with time for particle release at radial distance $r = 0.0041$ m. **d** Change in velocity with time for particle release at angular distance $r = 0.0041$ m

of maximum particle deposition is important for industrial application as it indicates the angles to avoid during pipe network design. Increased deposition may lead to increased pipe erosion and blockage.

Figure 7 shows the tracking of a single nanoparticle with time after release from a specified location in the flow field for 5% volume concentration at varying inclination angles. Significant changes in radial and angular position can be observed for lower angles of inclination which levels out at 90° inclination angle for both near-wall (Fig. 5a, b) and near-centre (Fig. 5c, d) nanoparticle release points. As mentioned above, the gravitational effect on nanoparticle motion is minimal compared to effects due to secondary flow. At 0°, secondary flows are dominant and they cause more drastic radial and angular movements of nanoparticles. However, at 90° the fluid flow is symmetrical and any secondary flows in the fluid approach uniformity across fluid cross section.

Intermediate angles of inclinations in Fig. 7a–d indicate time for the particle to stabilise decreases with an increase in inclination angle. In general, Fig. 7a, b also shows that nanoparticle released near the wall undergo deposition time $t_{\text{deposit}} \leq 40$ s after introduction into the fluid flow for inclination angles $0 \leq \alpha \leq 70°$ compared to $t_{\text{deposit}} \geq 50$ s for inclination angles of $70 \leq \alpha \leq 90°$. This means nanoparticles released near the wall are quickly deposited unless the inclination angle is close to 90°. This can be contrasted with Fig. 7c, d which shows nanoparticles with release

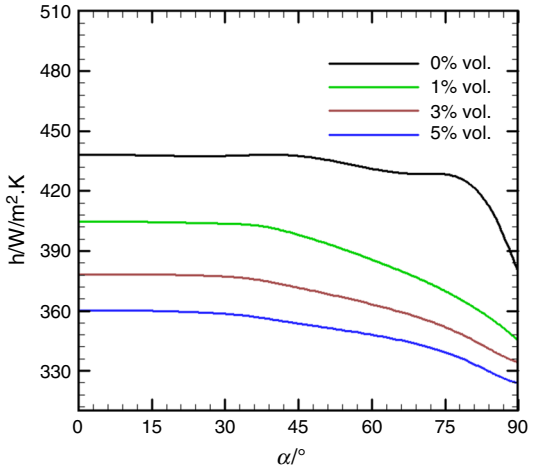

Fig. 9 Variation of heat transfer coefficient h with inclination angle α for particle volume concentrations 0–5%

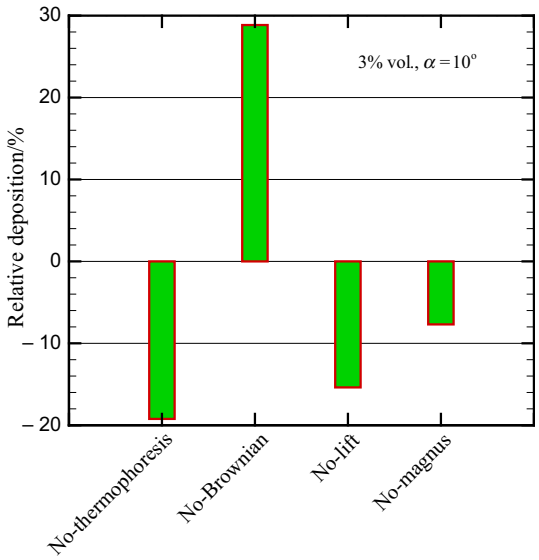

Fig. 10 Relative effect of thermophoresis, Brownian, Lift and Magnus forces on particle deposition for 3% volume concentration and inclination angle $\alpha = 10°$

points near the centre of fluid flow which has $t_{deposit} \leq 40$ s for inclination angles $\alpha \geq 30°$; that is, nanoparticles released near the centre are quickly captured when the inclination angle is greater than 30°. These results are important in informing design choices which seek to minimise nanoparticle deposition by optimising nanoparticle release points and inclination angles.

The changes in temperature and velocity of nanoparticles with time for varying inclination angles are shown in Fig. 8. After the initial adiabatic region where there is no temperature change, nanoparticle temperature reduces to approximately to 30 °C in less than 30 s. This behaviour is observed for both near-wall and near-centre particle release points and for all inclination angles unless deposition occurs. As suggested by Fig. 7, nanoparticles released near the wall and at high tube inclination angles achieve steady-state velocity after about 30 s, while nanoparticle released near the centre of fluid flow through low tube inclination angles achieve steady-state velocity after 30 s.

Figure 9 shows the effect of inclination angle on heat transfer coefficient (HTC). The HTC remains relatively constant until a critical angle, whereby increasing inclination angle further decreases the heat transfer coefficient. For particle volume concentration 1–5%, this occurs between $\alpha = 30°$ and $\alpha = 45°$. When the tube is horizontal ($\alpha = 0°$), there is a sharper reduction in the HTC that occurs at $\alpha \approx 80°$. The decrease in HTC can be attributed to increased gravity assisted flow, which leads to stronger convective flow and weaker secondary flow. It is worth noting that although Fig. 7 shows the decrease in HTC with particle volume concentration, it is possible that there exists a region of increasing HTC between 0 and 1%, where an optimum HTC value occurs in accordance with results by Ghodsinezhad et al. [35]. The determination of this optimum is beyond the scope of this study.

Figure 10 shows the effect of omitting the various forces included in the numerical analysis. It can be observed that all forces play a part in determining the nanoparticle behaviours in the fluid flow. However, the dominant forces were Brownian motion and thermophoresis which caused a difference of 28% and 18% in relative particle deposition, respectively, when individually omitted. This are a significant difference and outside acceptable error margins for similar numerical analysis. The omission of Brownian motion effect in the analysis increased particle deposition, while the omission of the Thermophoresis effect reduced relative particle deposition. This indicates that Brownian motion has a net dispersion effect on the nanoparticles from the wall as suggested by Eq. (26).

The dominant effect of Brownian motion is further emphasised in Fig. 11 which shows the effect of omitting different forces in the numerical analysis on the change in particle angular displacement with time. The only significant deviation in angular displacement curves occurs when Brownian effects are omitted from the analysis. From Fig. 11b, the omission of Brownian effects shows a significant

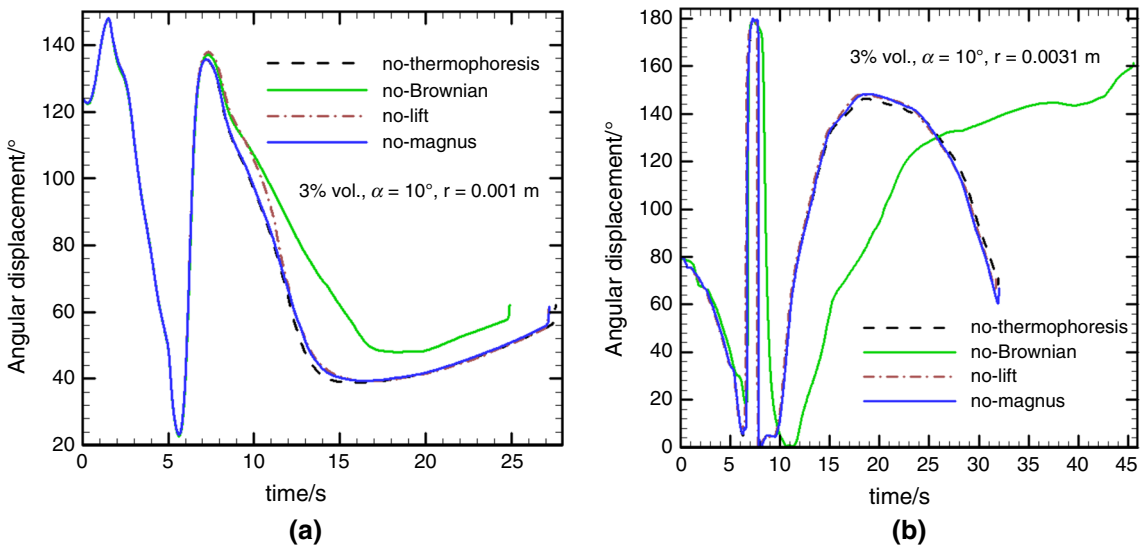

Fig. 11 Relative effect of thermophoresis, Brownian, Lift and Magnus forces on particle angular motion for 3% volume concentration and inclination angle $\alpha = 10°$ for particle release at radial distance. **a** $r = 0.0001$ m and **b** $r = 0.0031$ m

increase in deposition time $t_{deposit} \geq 45$ s com-pared to $t_{deposit} = 35$ s when included in the analysis.

Conclusions

This study has investigated the effect of varying inclination angles to nanoparticle migration and deposition in a fluid flow through a circular tube using the Eulerian–Lagrangian discrete phase model. Results have shown that inclination angle has a significant effect on nanoparticle distribution and there exists a critical angle where the nanoparticle deposition is maximised and found to be approximately 30°. Furthermore, the effect of inclination angle on the heat transfer coefficient was found to be minimal for angles 0° up to approximately 35° after which the HTC decreases with increasing inclination angle. Another finding of the study was the significance of the Brownian and thermophoresis effect on the particle deposition whereby the omission of these two effects resulted in a 28% and 18% difference in relative particle deposition result.

References

1. Hashemi M, Hossein S. Study of flow boiling heat transfer characteristics of critical heat flux using carbon nanotubes and water nanofluid. J Therm Anal Calorim. 2017;130:2199–209. https://doi.org/10.1007/s10973-017-6661-1.
2. Hemmat M, Seyfolah E. Turbulent forced convection heat transfer and thermophysical properties of MgO–water nanofluid with consideration of different nanoparticles diameter, an empirical study. J Therm Anal Calorim. 2015;119:1205–13. https://doi.org/10.1007/s10973-014-4197-1.
3. Mahdavi M, Sharifpur M, Ahmadi MH, Meyer JP. Aggregation study of Brownian nanoparticles in convective phenomena. J Therm Anal Calorim. 2018. https://doi.org/10.1007/s10973-018-7283-y.
4. Pinto RV, Fiorelli FAS. Review of the mechanisms responsible for heat transfer enhancement using nanofluids. Appl Therm Eng. 2016;108:720–39. https://doi.org/10.1016/j.applthermaleng.2016.07.147.
5. Omidi M, Farhadi M, Jafari M. A comprehensive review on double pipe heat exchangers. Appl Therm Eng. 2017;110:1075–90. https://doi.org/10.1016/j.applthermaleng.2016.09.027.
6. Mahdavi M, Sharifpur M, Meyer JP. CFD modelling of heat transfer and pressure drops for nanofluids through vertical tubes in laminar flow by Lagrangian and Eulerian approaches. Int J Heat Mass Transf. 2015;88:803–13. https://doi.org/10.1016/j.ijheatmasstransfer.2015.04.112.
7. Sharma S. Fabricating an experimental setup to investigate the performance of an automobile car radiator by using aluminum/water nanofluid. J Therm Anal Calorim. 2018;133:1387–406. https://doi.org/10.1007/s10973-018-7224-9.
8. Othman NA, Yacob NA, Bachok N, Ishak A, Pop I. Mixed convection boundary-layer stagnation point flow past a vertical stretching/shrinking surface in a nanofluid. Appl Therm Eng. 2016;115:1412–7. https://doi.org/10.1016/j.applthermaleng.2016.10.159.
9. Aberoumand S, Jafarimoghaddam A. Mixed convection heat transfer of nanofluids inside curved tubes: an experimental study. Appl Therm Eng. 2016;108:967–79. https://doi.org/10.1016/j.applthermaleng.2016.06.032.
10. Shamaeil M, Firouzi M, Fakhar A. The effects of temperature and volume fraction on the thermal conductivity of functionalized DWCNTs/ethylene glycol nanofluid. J Therm Anal Calorim. 2016;126:1455–62. https://doi.org/10.1007/s10973-016-5548-x.
11. Esfe MH, Saedodin S, Mahian O, Wongwises S. Thermal conductivity of Al_2O_3/water nanofluids: measurement, correlation, sensitivity analysis, and comparisons with literature reports.

J Therm Anal Calorim. 2014;117:675–81. https://doi.org/10.1007/s10973-014-3771-x.
12. Mahdavi M, Sharifpur M, Meyer JP. Simulation study of convective and hydrodynamic turbulent nanofluids by turbulence models. Int J Therm Sci. 2016;110:36–51. https://doi.org/10.1016/j.ijthermalsci.2016.05.027.
13. Behroyan I, Vanaki SM, Ganesan P, Saidur R. A comprehensive comparison of various CFD models for convective heat transfer of Al_2O_3 nanofluid inside a heated tube. Int Commun Heat Mass Transf. 2016;70:27–37.
14. Mokmeli A, Saffar-Avval M. Prediction of nanofluid convective heat transfer using the dispersion model. Int J Therm Sci. 2010;49:471–8. https://doi.org/10.1016/j.ijthermalsci.2009.09.005.
15. Dogonchi AS, Sheremet MA, Ganji DD, Pop I. Free convection of copper–water nanofluid in a porous gap between hot rectangular cylinder and cold circular cylinder under the effect of inclined magnetic field. J Therm Anal Calorim. 2018. https://doi.org/10.1007/s10973-018-7396-3.
16. Behzadmehr A, Galanis N. Prediction of turbulent forced convection of a nanofluid in a tube with uniform heat flux using a two phase approach. Int J Heat Fluid Flow. 2007;28:211–9. https://doi.org/10.1016/j.ijheatfluidflow.2006.04.006.
17. Ganesan P, Behroyan I, He S, Sivasankaran S, Sandaran SC, Behroyan I, He S, Sivasankaran S, Sandaran SC. Turbulent forced convection of Cu–water nanofluid in a heated tube: improvement of the two-phase model. Numer Heat Transf Part A Appl Int J Comput Methodol. 2016;69:401–20. https://doi.org/10.1080/10407782.2015.1081019.
18. Ding Y, Wen D. Particle migration in a flow of nanoparticle suspensions. Powder Technol. 2005;149:84–92. https://doi.org/10.1016/j.powtec.2004.11.012.
19. Aminfar H, Motallebzadeh R. Investigation of the velocity field and nanoparticle concentration distribution of nanofluid using Lagrangian–Eulerian approach. J Dispers Sci Technol. 2012;33:155–63. https://doi.org/10.1080/01932691.2010.528336.
20. Pakravan HA, Yaghoubi M. Combined thermophoresis, Brownian motion and Dufour effects on natural convection of nano fluids. Int J Therm Sci. 2011;50:394–402. https://doi.org/10.1016/j.ijthermalsci.2010.03.007.
21. Garoosi F, Rohani B, Rashidi MM. Two-phase mixture modeling of mixed convection of nanofluids in a square cavity with internal and external heating. Powder Technol. 2015;275:304–21. https://doi.org/10.1016/j.powtec.2015.02.015.
22. Buongiorno J. Convective transport in nanofluid. J Heat Transf. 2005;128:240–50. https://doi.org/10.1115/1.2150834.
23. Bianco V, Chiacchio F, Manca O, Nardini S. Numerical investigation of nanofluids forced convection in circular tubes. Appl Therm Eng. 2009;29:3632–42. https://doi.org/10.1016/j.applthermaleng.2009.06.019.
24. Keshavarz M, Esmaeili E. Comparison between single-phase and two-phases CFD modeling of laminar forced convection flow of nano fluids in a circular tube under constant heat flux. Int Commun Heat Mass Transf. 2012;39:1297–302. https://doi.org/10.1016/j.icheatmasstransfer.2012.07.012.
25. Mojarrad MS, Keshavarz A, Shokouhi A. Nanofluids thermal behavior analysis using a new dispersion model along with single-phase. Heat Mass Transf. 2013;49:1333–43. https://doi.org/10.1007/s00231-013-1182-3.
26. Kumar N, Puranik BP. Numerical study of convective heat transfer with nanofluids in turbulent flow using a Lagrangian–Eulerian approach. Appl Therm Eng. 2017;111:1674–81. https://doi.org/10.1016/j.applthermaleng.2016.08.038.
27. Zheng X, Silber-Li Z. The influence of Saffman lift force on nanoparticle concentration distribution near a wall. Appl Phys Lett. 2009;95:124105.
28. Saffman PGT. The lift on a small sphere in a slow shear flow. J Fluid Mech. 1965;22:385–400.
29. Li A, Ahmadi G. Dispersion and deposition of spherical particles from point sources in a turbulent channel flow. Aerosol Sci Technol. 1992;16:209–26. https://doi.org/10.1080/02786829208959550.
30. McNab GS, Meisen A. Thermophoresis in liquids. J Colloid Interface Sci. 1973;44:339–46. https://doi.org/10.1016/0021-9797(73)90225-7.
31. Oesterle B, Dinh TB. Experiments on the lift of a spinning sphere in a range of intermediate Reynolds numbers. Exp Fluids. 1998;25:16–22.
32. Apte SV, Mahesh K, Lundgren T. Accounting for finite-size effects in simulations of disperse particle-laden flows. Int J Multiphase Flow. 2008;34:260–71.
33. Oss CJVAN, Good RJ. Interfacial Lifshitz-van der Waals and polar interactions in macroscopic systems. Chem Rev. 1988;88:927–41.
34. Ben Mansour R, Galanis N, Nguyen CT. Experimental study of mixed convection with water–Al_2O_3 nanofluid in inclined tube with uniform wall heat flux. Int J Therm Sci. 2011;50:403–10. https://doi.org/10.1016/j.ijthermalsci.2010.03.016.
35. Ghodsinezhad H, Sharifpur M, Meyer JP. Experimental investigation on cavity flow natural convection of Al_2O_3–water nanofluids. Int Commun Heat Mass Transf. 2016;76:316–24. https://doi.org/10.1016/j.icheatmasstransfer.2016.06.005.